long, 10 mm in diameter) at 7×10^6 cells in 2 ml of complete DMEM. The test tubes with labeled cell suspensions were allowed to settle for 1 day to allow the cells to be precipitated before MR imaging. A test tube with unlabeled cell suspensions was also prepared in the same manner. In addition, a test tube with cell-free pure medium was prepared. The three test tubes prepared were arranged as shown in Fig. 4(a). Scanned slices were positioned so that they pass through the cell pellet part (slice B in Fig. 4a) or the solution part (slice A in Fig. 4a).

The cell density dependence of signal enhancement was examined as follows. Different numbers of labeled cells were suspended in 100 μl of agarose solution at the concentration of 2 wt% and cooled to be gelated. The MR imaging data of these mixtures were collected by a 1 T compact MR imaging system with a permanent magnet (MRmini, Dainippon Sumitomo Pharma, Osaka, Japan) with a *TE* of 9 ms and a *TR* of 1500 ms (FOV, 3 × 6 cm; matrix, 128 × 256; slice thickness, 3.7 mm).

5.11. *In vivo* fate of free SPIO and free Gd-PVA

The clearance of **4d** and SPIO after intramuscular injection was investigated in male rat F344. The rat was anesthetized by inhalation anesthesia (1.5% isoflurane). Solutions of **4d** (Gd 0.8 μmol per 50 μl water) and carboxydextran-coated SPIO, Resovist™ (Fe 0.8 μmol per 50 μl water, Bayer, Osaka, Japan) were injected into the left and right femoral muscles, respectively, using a 29 G needle. Whole inferior limbs of the animal were scanned at 0, 3 and 10 days after injection on a 1.5 T compact MR imaging system. These images were obtained with a *TR* of 1500 ms and a *TE* of 9 ms (FOV, 4 × 8 cm; matrix, 128 × 256; slice thickness, 1 mm; slice gap, 0 mm; number of slice, 35).

For the time course of the CNR and the number of voxels in the region, whole inferior limbs of the animal were scanned at 0, 1, 4, 6, 8, 11 and 13 days after injection on a 1.5 T compact MR imaging system. These images were obtained with a *TR* of 500 ms and a *TE* of 9 ms, and with a *TR* of 3000 ms and a *TE* of 20 ms (FOV, 4 × 8 cm; matrix, 128 × 256; slice thickness, 1 mm; slice gap, 0 mm; number of slices, 35). CNR was calculated as $(\pi/2)^{1/2}|S_1-S_2|/S_{air}$, where S_1, S_2 and S_{air} were the mean intensities in the contrast-enhanced region, muscle and air, respectively.

5.12. Preliminary MR imaging of transplanted NIH-3T3 cells

In vivo cell tracking was preliminarily performed in male Balb/c mice. These mice were anesthetized for imaging with the use of a general inhalation anesthesia (1.5% isoflurane) and were allowed to breathe spontaneously during preparation and scanning. NIH-3T3 cells labeled with **4d** (2×10^7 cells) were embedded in 2 wt% agarose gel (200 μl) and transplanted to the mice subcutaneously. MR images were obtained using a 2 T compact MR imaging system with a permanent magnet. T_1-weighted images were acquired using a 2D spin echo sequence with a *TR* of 2000 ms and a *TE* of 9 ms (FOV, 3 × 6 cm; matrix, 128 × 256; slice thickness, 1 mm) at room temperature.

6. SUPPORTING INFORMATION

Supporting information can be found in the online version of this article.

Acknowledgements

This work was supported by grants-in-aid from the Ministry of Health, Labour and Welfare of Japan (Health and Labour Sciences Research Grants, Research on Nanotechnical Medical). This work was also supported by a Research Grant for Cardiovascular Diseases (18A-2) from the Ministry of Health, Labour and Welfare of Japan.

References

1. Perin EC, Dohmann HF, Borojevic R, Silva SA, Sousa AL, Mesquita CT, Rossi MI, Carvalho AC, Dutra HS, Dohmann HJ, Silva GV, Belem L, Vivacqua R, Rangel FO, Esporcatte R, Geng YJ, Vaughn WK, Assad JA, Mesquita ET, Willerson JT., Transendocardial, autologous bone marrow cell transplantation for severe, chronic ischemic heart failure. Circulation 2003; 107 18 2294–2302.
2. Schmid C, Schleuning M, Schwerdtfeger R, Hertenstein B, Mischak-Weissinger E, Bunjes D, Harsdorf SV, Scheid C, Holtick U, Greinix H, Keil F, Schneider B, Sandherr M, Bug G, Tischer J, Ledderose G, Hallek M, Hiddemann W, Kolb HJ. Long-term survival in refractory acute myeloid leukemia after sequential treatment with chemotherapy and reduced-intensity conditioning for allogeneic stem cell transplantation. Blood 2006; 108(3): 1092–1099.
3. Slavin S, Nagler A, Naparstek E, Kapelushnik Y, Aker M, Cividalli G, Varadi G, Kirschbaum M, Ackerstein A, Samuel S, Amar A, Brautbar C, Ben-Tal O, Eldor A, Or R. Nonmyeloablative stem cell transplantation and cell therapy as an alternative to conventional bone marrow transplantation with lethal cytoreduction for the treatment of malignant and nonmalignant hematologic diseases. Blood 1998; 91(3): 756–763.
4. Kim SW, Han H, Chae GT, Lee SH, Bo S, Yoon JH, Lee YS, Lee KS, Park HK, Kang KS. Successful stem cell therapy using umbilical cord blood-derived multipotent stem cells for Buerger's disease and ischemic limb disease animal model. Stem Cells 2006; 24(6): 1620–1626.
5. Stamm C, Westphal B, Kleine HD, Petzsch M, Kittner C, Klinge H, Schumichen C, Nienaber CA, Freund M, Steinhoff G. Autologous bone-marrow stem-cell transplantation for myocardial regeneration. Lancet 2003; 361(9351): 45–46.
6. Strauer BE, Brehm M, Zeus T, Kostering M, Hernandez A, Sorg RV, Kogler G, Wernet P. Repair of infarcted myocardium by autologous intracoronary mononuclear bone marrow cell transplantation in humans. Circulation 2002; 106(15): 1913–1918.
7. Grant MB, May WS, Caballero S, Brown GA, Guthrie SM, Mames RN, Byrne BJ, Vaught T, Spoerri PE, Peck AB, Scott EW. Adult hematopoietic stem cells provide functional hemangioblast activity during retinal neovascularization. Nat Med 2002; 8(6): 607–612.
8. Tang YL, Zhao Q, Qin X, Shen L, Cheng L, Ge J, Phillips MI. Paracrine action enhances the effects of autologous mesenchymal stem cell transplantation on vascular regeneration in rat model of myocardial infarction. Ann Thorac Surg 2005; 80(1): 229–236 discussion 236-227.
9. Beeres SL, Bengel FM, Bartunek J, Atsma DE, Hill JM, Vanderheyden M, Penicka M, Schalij MJ, Wijns W, Bax JJ. Role of imaging in cardiac stem cell therapy. J Am Coll Cardiol 2007; 49(11): 1137–1148.
10. Frangioni JV, Hajjar RJ. In vivo tracking of stem cells for clinical trials in cardiovascular disease. Circulation 2004; 110(21): 3378–3383.
11. Tanaka M, Swijnenburg RJ, Gunawan F, Cao YA, Yang Y, Caffarelli AD, de Bruin JL, Contag CH, Robbins RC. In vivo visualization of cardiac allograft rejection and trafficking passenger leukocytes using bioluminescence imaging. Circulation 2005; 112(9 Suppl): I105–110.
12. Wang X, Rosol M, Ge S, Peterson D, McNamara G, Pollack H, Kohn DB, Nelson MD, Crooks GM. Dynamic tracking of human hematopoietic stem cell engraftment using in vivo bioluminescence imaging. Blood 2003; 102(10): 3478–3482.

13. Sutton EJ, Henning TD, Pichler BJ, Bremer C, Daldrup-Link HE. Cell tracking with optical imaging. Eur Radiol 2008; 18(10): 2021–2032.
14. Takagi Y, Takahashi J, Saiki H, Morizane A, Hayashi T, Kishi Y, Fukuda H, Okamoto Y, Koyanagi M, Ideguchi M, Hayashi H, Imazato T, Kawasaki H, Suemori H, Omachi S, Iida H, Itoh N, Nakatsuji N, Sasai Y, Hashimoto N. Dopaminergic neurons generated from monkey embryonic stem cells function in a Parkinson primate model. J Clin Invest 2005; 115(1): 102–109.
15. Takahashi M, Nakamura T, Toba T, Kajiwara N, Kato H, Shimizu Y. Transplantation of endothelial progenitor cells into the lung to alleviate pulmonary hypertension in dogs. Tissue Eng 2004; 10(5–6): 771–779.
16. Tomita S, Mickle DA, Weisel RD, Jia ZQ, Tumiati LC, Allidina Y, Liu P, Li RK. Improved heart function with myogenesis and angiogenesis after autologous porcine bone marrow stromal cell transplantation. J Thorac Cardiovasc Surg 2002; 123(6): 1132–1140.
17. Kraitchman DL, Tatsumi M, Gilson WD, Ishimori T, Kedziorek D, Walczak P, Segars WP, Chen HH, Fritzges D, Izbudak I, Young RG, Marcelino M, Pittenger MF, Solaiyappan M, Boston RC, Tsui BM, Wahl RL, Bulte JW. Dynamic imaging of allogeneic mesenchymal stem cells trafficking to myocardial infarction. Circulation 2005; 112(10): 1451–1461.
18. Hill JM, Dick AJ, Raman VK, Thompson RB, Yu ZX, Hinds KA, Pessanha BS, Guttman MA, Varney TR, Martin BJ, Dunbar CE, McVeigh ER, Lederman RJ. Serial cardiac magnetic resonance imaging of injected mesenchymal stem cells. Circulation 2003; 108(8): 1009–1014.
19. Rice HE, Hsu EW, Sheng H, Evenson DA, Freemerman AJ, Safford KM, Provenzale JM, Warner DS, Johnson GA. Superparamagnetic iron oxide labeling and transplantation of adipose-derived stem cells in middle cerebral artery occlusion-injured mice. AJR Am J Roentgenol 2007; 188(4): 1101–1108.
20. Stuckey DJ, Carr CA, Martin-Rendon E, Tyler DJ, Willmott C, Cassidy PJ, Hale SJ, Schneider JE, Tatton L, Harding SE, Radda GK, Watt S, Clarke K. Iron particles for noninvasive monitoring of bone marrow stromal cell engraftment into, and isolation of viable engrafted donor cells from, the heart. Stem Cells 2006; 24(8): 1968–1975.
21. Hoshino K, Ly HQ, Frangioni JV, Hajjar RJ. In vivo tracking in cardiac stem cell-based therapy. Prog Cardiovasc Dis 2007; 49(6): 414–420.
22. Amsalem Y, Mardor Y, Feinberg MS, Landa N, Miller L, Daniels D, Ocherashvilli A, Holbova R, Yosef O, Barbash IM, Leor J. Iron-oxide labeling and outcome of transplanted mesenchymal stem cells in the infarcted myocardium. Circulation 2007; 116(11 Suppl): I38–45.
23. Li Z, Suzuki Y, Huang M, Cao F, Xie X, Connolly AJ, Yang PC, Wu JC. Comparison of reporter gene and iron particle labeling for tracking fate of human embryonic stem cells and differentiated endothelial cells in living subjects. Stem Cells 2008; 26(4): 864–873.
24. Yamaoka T, Tabata Y, Ikada Y. Comparison of body distribution of poly(vinyl alcohol) with other water-soluble polymers after intravenous administration. J Pharm Pharmacol 1995; 47(6): 479–486.
25. Walczak P, Kedziorek DA, Gilad AA, Lin S, Bulte JW. Instant MR labeling of stem cells using magnetoelectroporation. Magn Reson Med 2005; 54(4): 769–774.
26. Pillai O, Panchagnula R. Polymers in drug delivery. Curr Opin Chem Biol 2001; 5(4): 447–451.
27. Li TS, Hamano K, Suzuki K, Ito H, Zempo N, Matsuzaki M. Improved angiogenic potency by implantation of ex vivo hypoxia prestimulated bone marrow cells in rats. Am J Physiol Heart Circ Physiol 2002; 283(2): H468–473.
28. Zhang S, Ge J, Zhao L, Qian J, Huang Z, Shen L, Sun A, Wang K, Zou Y. Host vascular niche contributes to myocardial repair induced by intracoronary transplantation of bone marrow CD34+ progenitor cells in infarcted swine heart. Stem Cells 2007; 25(5): 1195–1203.
29. Oude Engberink RD, van der Pol SM, Dopp EA, de Vries HE, Blezer EL., Comparison of SPIO and USPIO for in vitro labeling of human monocytes: MR detection and cell function. Radiology 2007; 243(2): 467–474.
30. Aime S, Cabella C, Colombatto S, Geninatti Crich S, Gianolio E, Maggioni F. Insights into the use of paramagnetic Gd(III) complexes in MR-molecular imaging investigations. J Magn Reson Imag 2002; 16(4): 394–406.
31. Gustafsson B, Youens S, Louie AY. Development of contrast agents targeted to macrophage scavenger receptors for MRI of vascular inflammation. Bioconjug Chem 2006; 17(2): 538–547.
32. Langereis S, de Lussanet QG, van Genderen MH, Meijer EW, Beets-Tan RG, Griffioen AW, van Engelshoven JM, Backes WH. Evaluation of Gd(III)DTPA-terminated poly(propylene imine) dendrimers as contrast agents for MR imaging. NMR Biomed 2006; 19(1): 133–141.
33. Lu ZR, Wang X, Parker DL, Goodrich KC, Buswell HR. Poly(-l-glutamic acid) Gd(III)–DOTA conjugate with a degradable spacer for magnetic resonance imaging. Bioconjug Chem 2003; 14(4): 715–719.
34. Nakamura E, Makino K, Okano T, Yamamoto T, Yokoyama M. A polymeric micelle MRI contrast agent with changeable relaxivity. J Control Release 2006; 114(3): 325–333.
35. Wen X, Jackson EF, Price RE, Kim EE, Wu Q, Wallace S, Charnsangavej C, Gelovani JG, Li C. Synthesis and characterization of poly(L-glutamic acid) gadolinium chelate: a new biodegradable MRI contrast agent. Bioconjug Chem 2004; 15(6): 1408–1415.
36. Yan GP, Liu ML, Li LY. Polyaspartamide gadolinium complexes containing sulfadiazine groups as potential macromolecular MRI contrast agents. Bioconjug Chem 2005; 16(4): 967–971.
37. Yamaoka T, Tabata Y, Ikada Y. Distribution and tissue uptake of poly(ethylene glycol) with different molecular weights after intravenous administration to mice. J Pharm Sci 1994; 83(4): 601–606.
38. Yamaoka T, Tabata Y, Ikada Y. Fate of water-soluble polymers administered via different routes. J Pharm Sci 1995; 84(3): 349–354.

Timing-controlled Decompaction of Polyplexes In Vivo Greatly Enhances Transgene Expression

Yoichi Tachibana,[1] Tomoko Hashimoto,[1,2] Hisae Nozaki,[1] Akira Murakami,[2] and Tetsuji Yamaoka[1]
[1]*Department of Biomedical Engineering, National Cerebral and Cardiovascular Center Research Institute, Fujishirodai, Suita, Osaka 565-8585*
[2]*Department of Biomolecular Engineering, Kyoto Institute of Technology, Matsugasaki, Sakyo-ku, Kyoto 606-8585*

(Received September 8, 2010; CL-100773; E-mail: yamtet@ri.ncvc.go.jp)

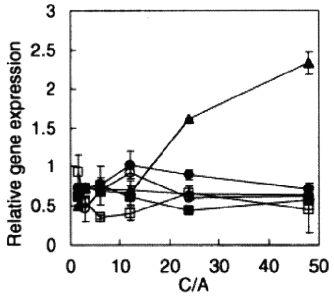

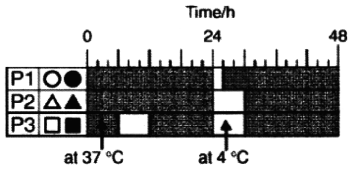

REPRINTED FROM

Chemistry Letters

Vol.39 No.12 2010 p.1238–1239
CMLTAG
December 5, 2010

The Chemical Society of Japan

Published on the web October 23, 2010; doi:10.1246/cl.2010.1238

doi:10.1246/cl.2010.1238
1238 Published on the web October 23, 2010

Timing-controlled Decompaction of Polyplexes In Vivo Greatly Enhances Transgene Expression

Yoichi Tachibana,[1] Tomoko Hashimoto,[1,2] Hisae Nozaki,[1] Akira Murakami,[2] and Tetsuji Yamaoka[1]
[1]*Department of Biomedical Engineering, National Cerebral and Cardiovascular Center Research Institute, Fujishirodai, Suita, Osaka 565-8585*
[2]*Department of Biomolecular Engineering, Kyoto Institute of Technology, Matsugasaki, Sakyo-ku, Kyoto 606-8585*

(Received September 8, 2010; CL-100773; E-mail: yamtet@ri.ncvc.go.jp)

Compaction extent of polyplexes was successfully regulated by cold treatment in buffer solution using thermoresponsive gene carriers composed of linear poly(ethyleneimine) (l-PEI) and alkyl side chains. Plasmid DNA (pCMV-Luc) was transfected to COS-1 cells using these carriers with different cold treatments. The luciferase expression was greatly enhanced when cells were treated at 4 °C in well-defined timing. This was a direct observation of how intracellular destabilization in regulated timing is important for nonviral gene transfection.

There has been significant interest in synthetic polycation as a non-viral gene carrier and in gene therapy.[1] Several polycationic carriers, such as poly(ethyleneimine) (PEI),[2] poly(L-lysine) (PLL),[3] and chitosan,[4] have been developed due to various advantages over viral vectors. Among them, PEI is one of the most widely studied gene carriers because of its high efficiency gene expression.[2] Furthermore, mechanism analysis for efficient gene transfer including cellular uptake, lysosomal escape, and nuclear transport has been widely carried out. Although the decompaction or dissociation of polyplexes is believed to be important for gene expression, studies of this are not well developed because it is not easy to control these phenomena in cells.

Recently, thermoresponsive polymers have received much attention as intelligent materials for various applications. Poly(*N*-isopropylacrylamide) (PNIPAAm) is one of the most typical thermoresponsive polymers.[5] A block copolymer consisting of poly(L-lactic acid) and poly(ethylene glycol)[6] and poly(amino acid)s[7] have been also reported. Kurisawa et al. reported that thermoresponsive copolymer, poly[*N*-isopropylacrylamide-*co*-2-(dimethylamino)ethyl methacrylate-*co*-butyl methacrylate], showed high transfection efficiency.[8,9] A PEI-*graft*-PNIPAAm copolymer was synthesized as a thermoresponsive carrier by Bisht et al.[10] Lavigne et al. reported that high gene expression using PEI–PNIPAAm conjugates as a carrier occurred below the LCST.[11] We report herein synthesis and timing-controlled gene transfection by use of new thermoresponsive PEI derivatives as gene carriers. PEI derivatives were synthesized by the reaction of l-PEI ($M_w = 22000$) with various carboxylic acid chlorides in chloroform at room temperature for 48 h (Scheme 1). In this study, butyryl chloride, propanoyl chloride, and hexanoyl chloride were used for the synthesis of PEI derivatives. The synthesis of PEI derivatives is summarized in Table 1 and the introduction ratio was determined by ^{1}H NMR. PEI-C4 was soluble in water at room temperature. PEI-C5 and PEI-C6 were insoluble in water.

Figure 1 shows the transfection efficiency of PEI derivative/pCMV-Luc complexes. Complexes were formed by mixing PEI derivatives with pCMV-Luc at several cation/anion (C/A) ratios. The transfection efficiency was determined by luciferase activity in COS-1 cells at 37 °C. PEI homopolymer as a control showed high transfection efficiency with increasing C/A ratio. The transfection efficiency of PEI-C4 at high C/A ratios of 24 and 48 was almost the same as that of PEI. It was demonstrated that the transfection efficiency was not affected by the introduction into the side chain of PEI. For PEI-C5 and PEI-C6, low transfection efficiencies were observed because of their low solubility in water.

Figure 2 shows photographs of 1 wt % solution of PEI-C4 at 4 and 37 °C. The transparent solution at 4 °C became opaque at 37 °C. The turbidity change took place sharply in both heating and cooling processes. This result showed that PEI-C4 was

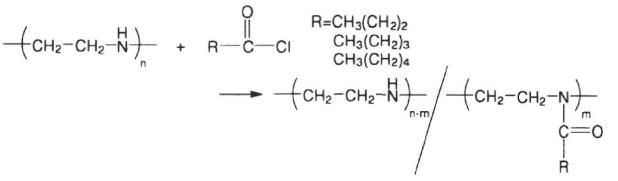

Scheme 1.

Table 1. Synthesis of PEI derivatives

Sample	Chloride	Yield/%	Introduction ratio[a]/%
PEI-C4	Butyryl chloride	55	64
PEI-C5	Propanoyl chloride	64	67
PEI-C6	Hexanoyl chloride	59	58

[a]Determined by ^{1}H NMR.

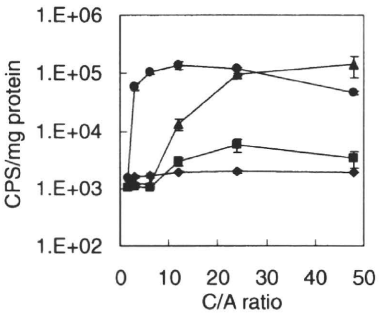

Figure 1. Transfection efficiency determined by luciferase activity in COS-1 at 37 °C. The polyplexes composed of pCMV-Luc (100 ng) and polycations (C/A 48–1.5) in FBS (−) DMEM were added to culture medium for 1×10^4 cells per well in the presence of 100 μM chloroquine. ●: PEI, ▲: PEI-C4, ■: PEI-C5, and ◆: PEI-C6. Values are shown as means ± standard deviations.

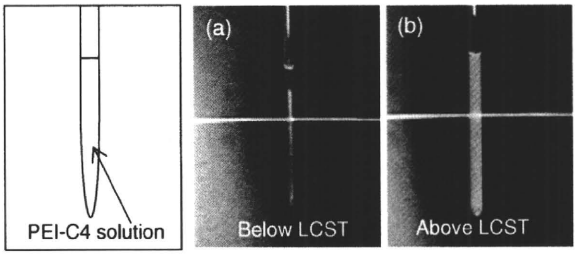

Figure 2. Photographs of the 1 wt % polymer solution of PEI-C4 at (a) 4 and (b) 37 °C.

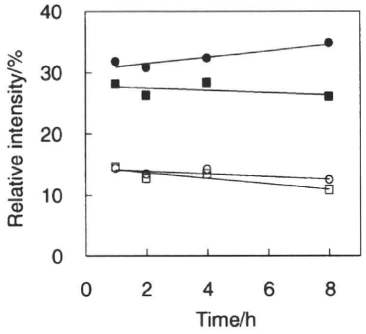

Figure 3. Relative fluorescence intensities of complexes depending on the temperature. Fluorescein-labeled plasmid DNA was complexed with PEI or PEI-C4. Complexes were incubated at 4 or 37 °C for various times. ●: PEI-C4 (4 °C), ■: PEI-C4 (37 °C), ○: PEI (4 °C), and □: PEI (37 °C).

thermoresponsive polymer. The LCST of PEI-C4 was estimated around 30 °C.

Relative fluorescence intensities of complexes depending on the temperature were examined (Figure 3). Fluorescein-labeled pCMV-Luc (F-pCMV-Luc) was complexed with PEI or PEI-C4 at the C/A ratio of 24 and complexes were incubated at 4 or 37 °C for 1, 2, 4, and 8 h. A gradual increase in the relative fluorescence intensity of PEI-C4/F-pCMV-Luc complex by treating at 4 °C was found, whereas such increase was not observed when the complex was incubated at 37 °C. In the case of PEI, the change of relative fluorescence intensities was not observed. This change must be because of the decompaction of the polyplexes resulting from the increased hydrophilicity of the PEI-C4. The temperature lower than the LCST caused a conformational change of PEI-C4 and made the complex unstable.

Effects of the post-transfection cold procedure on the luciferase expression are shown in Figure 4B. Relative gene expression was calculated as follows: (CPS/mg protein with the cooling procedure)/(CPS/mg protein without the cooling procedure). When cells were treated at 4 °C for 6 h at 24 h post transfection, the relative gene expression increased 2.3 times (Figure 4A, ▲). This kind of enhancement was not observed for the PEI (Figure 4A, open marks). The cold treatment for 2 h did not affect the expression at all (Figure 4A, ●). This may be due to insufficient decompaction of the polyplexes. The internalized complexes are considered to be decompacted as is shown in Figure 3 and were transcribed, resulting in high gene expression. When cells were cold treated for 6 h at 6 h post transfection, the

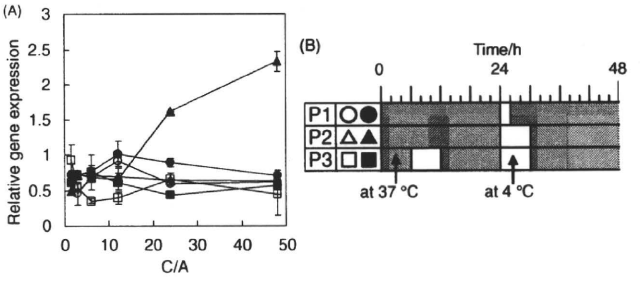

Figure 4. Relative gene expression depending on temperature (A). Cells were incubated with complexes composed of pCMV-Luc (100 ng) and polycations (C/A 48–1.5) in FBS (−) DMEM. PEI-C4 (closed symbol) and PEI (open symbol) were used. The cooling procedure is shown on panel B.

expression enhancement was not observed even for the 6 h cold treatment at 24 h post transfection (Figure 4A, ■), suggesting that the decompaction at a too early stage in the intracellular trafficking of polyplexes suppressed the gene expression completely.

In conclusion, new thermoresponsive polymers based on PEI were used for controlling the intracellular decompaction of the polyplexes. Thermoresponse was found in polymer solution prepared by the reaction of butyryl chloride with PEI. The stability of PEI-C4/F-pCMV-Luc complex was clearly affected by cold treatment in a buffer solution. Furthermore, high gene expression was achieved by well-defined cold treatment procedure. Our system will be useful for mechanistic analysis of the intracellular behavior of polyplexes for efficient polymeric carrier-based gene transfer.

This work was supported by Grants-in-Aid from the Ministry of Health, Labour and Welfare of Japan and by the Program for Promotion of Fundamental Studies in Health Sciences of National Institute of Biomedical Innovation of Japan.

References

1 a) A. V. Kabanov, V. A. Kabanov, *Bioconjugate Chem.* **1995**, *6*, 7. b) T. Hashimoto, Y. Tachibana, H. Nozaki, O. Mazda, T. Niidome, A. Murakami, T. Yamaoka, *Chem. Lett.* **2009**, *38*, 718.
2 W. T. Godbey, K. K. Wu, A. G. Mikos, *J. Controlled Release* **1999**, *60*, 149.
3 V. Toncheva, M. A. Wolfert, P. R. Dash, D. Oupicky, K. Ulbrich, L. W. Seymour, E. H. Schacht, *Biochim. Biophys. Acta* **1998**, *1380*, 354.
4 T. H. Kim, I. K. Park, J. W. Nah, Y. J. Choi, C. S. Cho, *Biomaterials* **2004**, *25*, 3783.
5 M. Heskins, J. E. Guillet, *J. Macromol. Sci., Part A: Pure Appl. Chem.* **1968**, *2*, 1441.
6 T. Fujiwara, T. Mukose, T. Yamaoka, H. Yamane, S. Sakurai, Y. Kimura, *Macromol. Biosci.* **2001**, *1*, 204.
7 a) Y. Tachibana, M. Kurisawa, H. Uyama, T. Kakuchi, S. Kobayashi, *Chem. Commun.* **2003**, 106. b) Y. Tachibana, M. Kurisawa, H. Uyama, S. Kobayashi, *Biomacromolecules* **2003**, *4*, 1132.
8 B. R. Twaites, C. de las Heras Alarcón, D. Cunliffe, M. Lavigne, S. Pennadam, J. R. Smith, D. C. Górecki, C. Alexander, *J. Controlled Release* **2004**, *97*, 551.
9 a) M. Kurisawa, M. Yokoyama, T. Okano, *J. Controlled Release* **2000**, *68*, 1. b) M. Kurisawa, M. Yokoyama, T. Okano, *J. Controlled Release* **2000**, *69*, 127. c) M. Yokoyama, M. Kurisawa, T. Okano, *J. Artif. Organs* **2001**, *4*, 138.
10 H. S. Bisht, D. S. Manickam, Y. You, D. Oupicky, *Biomacromolecules* **2006**, *7*, 1169.
11 M. D. Lavigne, S. S. Pennadam, J. Ellis, L. L. Yates, C. Alexander, D. C. Górecki, *J. Gene Med.* **2007**, *9*, 44.

Eur J Nucl Med Mol Imaging (2010) 37:377–385
DOI 10.1007/s00259-009-1262-2

ORIGINAL ARTICLE

Quantification of regional myocardial oxygen metabolism in normal pigs using positron emission tomography with injectable ^{15}O-O_2

Takashi Temma · Hidehiro Iida · Takuya Hayashi · Noboru Teramoto · Youichiro Ohta · Nobuyuki Kudomi · Hiroshi Watabe · Hideo Saji · Yasuhiro Magata

Received: 27 April 2009 / Accepted: 10 August 2009 / Published online: 4 September 2009

Abstract
Purpose Although ^{15}O-O_2 gas inhalation can provide a reliable and accurate myocardial metabolic rate for oxygen by PET, the spillover from gas volume in the lung distorts the images. Recently, we developed an injectable method in which blood takes up ^{15}O-O_2 from an artificial lung, and this made it possible to estimate oxygen metabolism without the inhalation protocol. In the present study, we evaluated the effectiveness of the injectable ^{15}O-O_2 system in porcine hearts.
Methods PET scans were performed after bolus injection and continuous infusion of injectable ^{15}O-O_2 via a shunt between the femoral artery and the vein in normal pigs. The injection method was compared to the inhalation method. The oxygen extraction fraction (OEF) in the lateral walls of the heart was calculated by a compartmental model in view of the spillover and partial volume effect.
Results A significant decrease of lung radioactivity in PET images was observed compared to the continuous inhalation of ^{15}O-O_2 gas. Furthermore, the injectable ^{15}O-O_2 system provides a measurement of OEF in lateral walls of the heart that is similar to the continuous-inhalation method (0.71 ± 0.036 and 0.72 ± 0.020 for the bolus-injection and continuous-infusion methods, respectively).
Conclusion These results indicate that injectable ^{15}O-O_2 has the potential to evaluate myocardial oxygen metabolism.

Keywords Myocardial oxygen metabolism · PET · Pig · OEF · Injectable ^{15}O-O_2

T. Temma · H. Saji
Department of Patho-Functional Bioanalysis,
Graduate School of Pharmaceutical Sciences, Kyoto University,
Kyoto, Japan

H. Iida · T. Hayashi · N. Teramoto · Y. Ohta · N. Kudomi · H. Watabe
Department of Investigative Radiology,
National Cardiovascular Center Research Institute,
Osaka, Japan

Y. Magata (✉)
Laboratory of Genome Bio-Photonics,
Photon Medical Research Center,
Hamamatsu University School of Medicine,
1-20-1 Handayama,
Hamamatsu 431-3192, Japan
e-mail: magata@hama-med.ac.jp

Introduction

In the myocardium, fatty acid or glucose is used to produce energy by aerobic metabolism. Oxygen is one of the most important substrates closely related to the aerobic metabolism in the TCA cycle; thus, oxygen metabolism should be a direct reflection of myocardial metabolism of these substrates. Therefore, there has been considerable interest in the development of a method to quantify oxygen metabolism in the myocardium.

Recently, ^{11}C-acetate has been used for this purpose [1–5]. ^{11}C-acetate is taken up by the mitochondria and metabolically converted into acetyl-CoA. It then enters the TCA cycle and is transformed to ^{11}C-CO_2, which is cleared rapidly from the myocardium. Thus, the clearance pharmacokinetics reflects oxygen metabolism in the myocardium. However, the quantification of oxygen metabolism using ^{11}C-acetate is quite difficult because of various intermediary compounds.

The use of ^{15}O-O_2 gas inhalation and PET scanning can provide a quantitative myocardial metabolic rate for oxygen ($MMRO_2$) [6, 7]. The tracer kinetic model used is based on that originally proposed to describe the behavior of ^{15}O-O_2 in brain tissue [8, 9]. However, the direct translation of the

compartmental model for the brain to the heart is not permitted, because subtraction for spillover from gas volume in addition to that from the blood pool is needed. A previous study demonstrated that the gas volume can be accurately estimated from the transmission scan data; thus, this technique did not require additional emission scanning for estimating the quantitative gas volume images [6, 7]. However, gaseous radioactivity in the lung during the inhalation of ^{15}O-O_2 gas is too high in comparison to other regions. Subtraction for this contribution is straightforward and accurate using the transmission scan-derived gaseous volume images, but the lung radioactivity degraded image quality in the estimated $MMRO_2$ images.

As an alternative to gas inhalation, we recently developed a method to prepare an injectable form of ^{15}O-O_2. This was accomplished by exposing pre-collected blood to ^{15}O-O_2 gas using a small artificial lung system resulting in a maximum yield of 130 MBq/ml. We demonstrated that cerebral oxygen metabolism could be estimated in normal and ischemic rats using injectable ^{15}O-O_2 [10–12]. This technique has the potential of avoiding the inhalation protocol.

The aim of the present study was therefore to test the feasibility of using the injectable ^{15}O-O_2 oxygen system for estimating myocardial oxygen metabolism in pigs. The injection method was compared to the inhalation method to determine if the injection method resulted in a reduction of lung radioactivity, an improved image quality, a more accurate estimate of myocardial oxygen metabolism, and an improved signal-to-noise ratio.

Materials and methods

Theory

^{15}O-Oxygen was administered by IV injection or inhalation and was carried as ^{15}O-hemoglobin by blood to peripheral tissues including the myocardium, where it was converted to ^{15}O-water (^{15}O-H_2O_{met}) through aerobic metabolism. The increased distribution volume of ^{15}O-H_2O_{met}, represented by the exchangeable water space of tissue, causes delayed removal of radioactivity. This allows the definition of an appropriate model and equations to be derived for the calculation of a regional myocardial metabolic rate for oxygen ($rMMOR_2$) and regional oxygen extraction fraction (rOEF). Previous studies demonstrated that these calculations were similar to those used for estimating cerebral blood flow and oxygen metabolism and require the measurement of regional myocardial blood flow (rMBF) and a correction for spillover of activity from the vascular pools and the pulmonary alveoli [6, 7]. rMBF was measured by the ^{15}O-H_2O injection technique [13]. Activity in the vascular pools of the heart chambers and the lung was evaluated with a conventional measurement of blood volume using ^{15}O-CO, and activity in the pulmonary alveoli was evaluated with an unconventional and indirect measurement of gas volume obtained from the transmission scan. Furthermore, the existence of recirculating ^{15}O-H_2O_{met} in the blood freely accessible to the myocardium was taken into consideration.

The differential equation describing the myocardial kinetics after administration of ^{15}O-O_2 can be written as follows:

$$\frac{dC^{myo}(t)}{dt} = OEF \cdot f \cdot A_o(t) + f \cdot A_w(t) - \left(\frac{f}{p} + \lambda\right) C^{myo}(t) \quad (1)$$

where $C^{myo}(t)$ designates the true radioactivity concentration in the myocardium at time t, f is myocardial blood flow, $A_O(t)$ is the ^{15}O-O_2 radioactivity concentration in arterial blood, $A_W(t)$ is the ^{15}O-H_2O radioactivity concentration in arterial blood, p is the myocardium/blood partition coefficient of water, and λ is the physical decay constant of O-15.

Solving Eq. (1) in terms of $C^{myo}(t)$ gives:

$$C^{myo}(t) = OEF \cdot f \cdot A_o(t) * e^{-\left(\frac{f}{p}+\lambda\right)\cdot t} + f \cdot A_w(t) * e^{-\left(\frac{f}{p}+\lambda\right)\cdot t} \quad (2)$$

where the asterisk denotes the convolution integral. During steady-state conditions under the continuous administration of ^{15}O-O_2, the following relationship holds:

$$C^{myo} = \frac{OEF \cdot f \cdot A_o + f \cdot A_w}{\left(\frac{f}{p} + \lambda\right)} \quad (3)$$

In the actual PET studies, the spillover from vascular pools and pulmonary alveoli and the partial volume effect should be taken into consideration [14]. Then, the measured radioactivity concentration in the region of interest (ROI) in the myocardium ($R^{myo}(t)$) can be expressed as:

$$\begin{aligned} R^{myo}(t) = {} & \alpha \cdot C^{myo}(t) \\ & + (V_B^{myo} \cdot A_t(t) - \alpha \cdot F_{Vein} \cdot OEF \cdot A_o(t) - \alpha \cdot F_{Vein} \cdot A_w(t)) \\ & + V_G^{myo} \cdot C_{gas}(t) \end{aligned} \quad (4)$$

where α denotes the myocardial tissue fraction, V_B^{myo} is the myocardial blood volume, $A_t(t)$ is the total O-15 radioactivity concentration in arterial blood, F_{vein} is the microscopic venous blood volume, V_G^{myo} is the gas volume in the myocardial ROI and $C_{gas}(t)$ is the O-15 radioactivity concentration in V_G^{myo}.

With the bolus injection or infusion methods using an artificial lung system, the radioactivity in the pulmonary alveoli is expected to be negligible in comparison with the inhalation method. Thus, Eq. (4) can be converted to:

$$R^{myo}(t) = \alpha \cdot C^{myo}(t) + (V_B^{myo} \cdot A_t(t) - \alpha \cdot F_{Vein} \cdot OEF \cdot A_o(t) - \alpha \cdot F_{Vein} \cdot A_w(t)) \quad (5)$$

Subjects

In this study, four healthy miniature pigs (22–30 kg) were used. The pigs were anesthetized by IM injection of ketamine and xylazine followed by continuous infusion of propofol (5 mg/kg/h). The animals were then placed in the supine position on the bed of the PET scanner. All experimental procedures were approved by the local animal welfare committee.

Injectable ^{15}O-O_2 preparation

In the "injection" study, injectable ^{15}O-O_2 was used. Injectable ^{15}O-O_2 was prepared as described previously [10–12]. In brief, part of an infusion line kit (Terumo Corporation, Tokyo, Japan) and an artificial lung 18 cm in length (Senko Medical Instrument Mfg Co. Ltd., Tokyo, Japan) were connected using silicone tubing to make a closed system. Then, venous blood collected from a pig, which was used in the following PET studies, was added to the system and circulated (100 ml/min) by a peristaltic pump, followed by introduction of ^{15}O–O_2 gas (~7,000 MBq/min/433 ml) into the artificial lung for 15 min to prepare injectable ^{15}O-O_2 (5.6–60.7 MBq/ml).

In the "continuous infusion" study, the left femoral artery and right femoral vein were both cannulated. The two cannulas from the artery and the vein were connected to the opposite sides of an artificial lung to create a femoral shunt. The blood flow in the shunt was aided by a peristaltic pump (30–50 ml/min). ^{15}O-O_2 gas (~7,000 MBq/min/433 ml) was continuously introduced into the artificial lung.

PET protocol (Fig. 1)

The PET scanner was an ECAT EXACT HR (CTI/Siemens) [15], which has an imaging field of view (FOV) of 55 cm in diameter and 15 cm in axial length. The spatial resolution of the scanner is 5.8 mm in full width at half maximum at the center of the FOV.

After obtaining a 20-min transmission scan for attenuation correction and gas volume estimation, the blood pool image was obtained with a 4-min PET scan after the pigs inhaled 2.7 GBq ^{15}O-CO for 30 s. Arterial blood samples were taken every minute during the ^{15}O-CO scanning, and

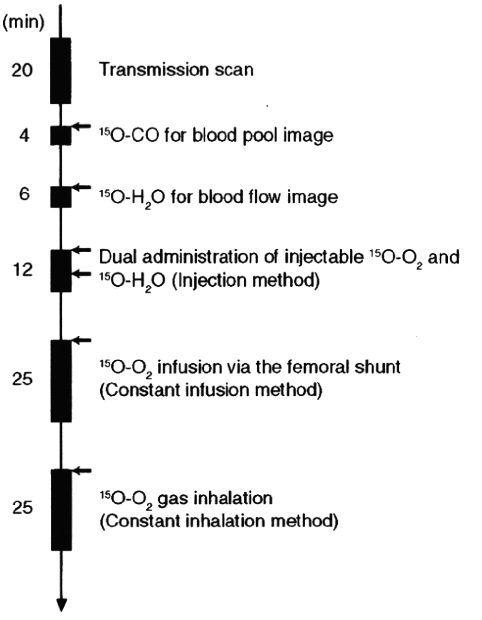

Fig. 1 Outline of the PET imaging study. The interval between scans was more than 15 min to allow for physical decay of O-15 radioactivity to background levels

the radioactivity concentration in the whole blood was measured with a NaI well-type scintillation counter calibrated against the PET scanner. Subsequently, ^{15}O-water was injected into the right femoral vein for 30 s at an infusion rate of 10 ml/min (injected radioactivity was about 1.11 GBq). Immediately after injection of ^{15}O-water, 26 dynamic frames (12×5 s, 8×15 s and 6×30 s) of PET data were acquired for 6 min.

Furthermore, two PET scans were successively performed after the IV injection of ^{15}O-O_2 (5.6–60.7 MBq/ml) for 30 s at an injection rate of 20–80 ml/min for the "injection" study, and by the continuous ^{15}O-O_2 gas infusion through the artificial lung in the femoral shunt for the "continuous infusion" study. In the "injection" study, 52 dynamic frames (12×5 s, 8×15 s, 6×30 s, 12×5 s, 8×15 s and 6×30 s) of PET data were acquired for 12 min, and 1.11 GBq of ^{15}O-water was injected IV for 30 s at 10 ml/min starting at 6 min after the administration of IV ^{15}O-O_2 according to the dual administration protocol we developed previously [16]. In the "continuous infusion" study, 26 dynamic frames (10×30 s, 5×60 s, 1×600 s and 10×30 s) were acquired for 25 min, and the 600-s frame was used for steady-state analysis.

Another PET scan was performed by ^{15}O-O_2 gas inhalation in one of the four pigs in the same protocol as the "continuous infusion" study. This was the "continuous inhalation" study. The interval between scans was more

than 15 min to allow for physical decay of O-15 radioactivity to background levels. All acquisitions were obtained in the two-dimensional mode (septa extended).

Data analysis

A filtered back-projection algorithm with a 6-mm Gaussian filter was used for image reconstruction. The reconstructed images had a matrix size of 128 × 128 × 47 and a voxel size of 1.84 × 1.84 × 3.38 mm, and all image data sets were resliced into short-axis images across the left ventricle [13].

Myocardial blood flow

rMBF was calculated from the injection of ^{15}O-H_2O by fitting the myocardial and arterial time-activity curve data to a single-tissue-compartment model that implemented corrections for partial-volume effects by introducing the tissue fraction. In addition, the model was corrected for spillover from the left ventricular (LV) chamber into the myocardial ROI by introducing the arterial blood volume [13]. In these experiments, the time-activity curves generated from large ROIs placed in the LV chamber were used as the input function.

Regional oxygen extraction fraction

In the "injection" study, rOEF was calculated according to Eqs. (2) and (5). In these formulations, F_{vein} was assumed to be 0.10 ml/g tissue and p was fixed at 0.90 ml/g. The blood volume image obtained from the ^{15}O-CO scan was used for the determination of V_B^{myo}. The value of $A_t(t)$ was obtained from the LV radioactivity concentration measured from the PET data set with small LV ROIs to minimize spillover from the myocardium. The calculation for the estimation of recirculating ^{15}O-H_2O was performed as previously described [16]. For the "continuous infusion" and "continuous inhalation" studies, in which a 600-s frame was regarded as steady-state, Eqs. (3) and (5) or Eqs. (3) and (4) were used for calculating rOEF, respectively.

Results

Table 1 summarizes the conditions of animals during the PET studies. The parameters were all within the physiologic range.

Figure 2 demonstrates the dynamic images obtained in the "injection", "continuous infusion", and "continuous inhalation" studies. With the injection and continuous-infusion methods, the right ventricle on the left side and the vena cava on the lower side were well delineated, whereas the left ventricle was moderately shown on the right side. The 16th frame (600~1,200 s after the initiation), which was used for steady-state analysis with the continuous-infusion method, was visibly distinct compared with all of the frames obtained with the injection method. However, with the continuous-inhalation method, neither ventricle could be depicted because of high radioactivity in the lung on the right and lower-side images.

The radioactivity in the blood pool obtained by ^{15}O-CO PET (Fig. 3g) and the gaseous volume estimated by inverse transmission data (Fig. 3h) were subtracted from the raw PET images (16th frame) with the continuous-inhalation and continuous-infusion methods, respectively (Fig. 3c and f). Both methods clearly delineated the myocardium after subtraction in comparison to the blood flow image (Fig. 3i). However, the continuous-inhalation method showed salient radioactivity on the lateral wall (Fig. 3c), whereas the continuous-infusion method showed only modest radioactivity in the myocardium (Fig. 3f). It is also notable that there was considerable radioactivity in the right ventricle with the continuous-infusion method even after the subtraction (Fig. 3f).

To further examine the differences between the continuous-infusion and continuous-inhalation methods, time-radioactivity curves during the PET scans were taken from four ROIs: the left ventricle (LV), right ventricle (RV), myocardium (Myo), and lung (Fig. 4). At the steady-state frame (600~1,200 s), the continuous-infusion method showed higher radioactivity in the RV and LV than in the myocardium (Fig. 4a), whereas the radioactivity of these regions was similar with the continuous-inhalation method (Fig. 4b). The radioactivity in LV was about two-thirds of that in RV in Fig. 4a, indicating that measurable radioactivity was excreted through the lung even after the femoral administration of ^{15}O-O_2. The lung excretion was also observed on the blood-subtracted image (Fig. 3e). Actually, there was significant radioactivity in the lung (Fig. 4a), although that was the lowest among the four ROIs. In contrast, the radioactivity in the myocardium was the lowest among the four ROIs with the continuous-inhalation method

Table 1 Physiological parameters of pigs during the PET studies

	pH	pCO_2 (mmHg)	pO_2 (mmHg)	tHb (g/dl)	O_2Sat (%)	HR (bpm)	BP (mmHg)	
							Diastolic	Systolic
Average	7.46	40.3	125.8	12.8	97.7	85	97.8	125.2
SD	0.032	2.51	16.69	1.30	1.83	19.5	10.4	19.3

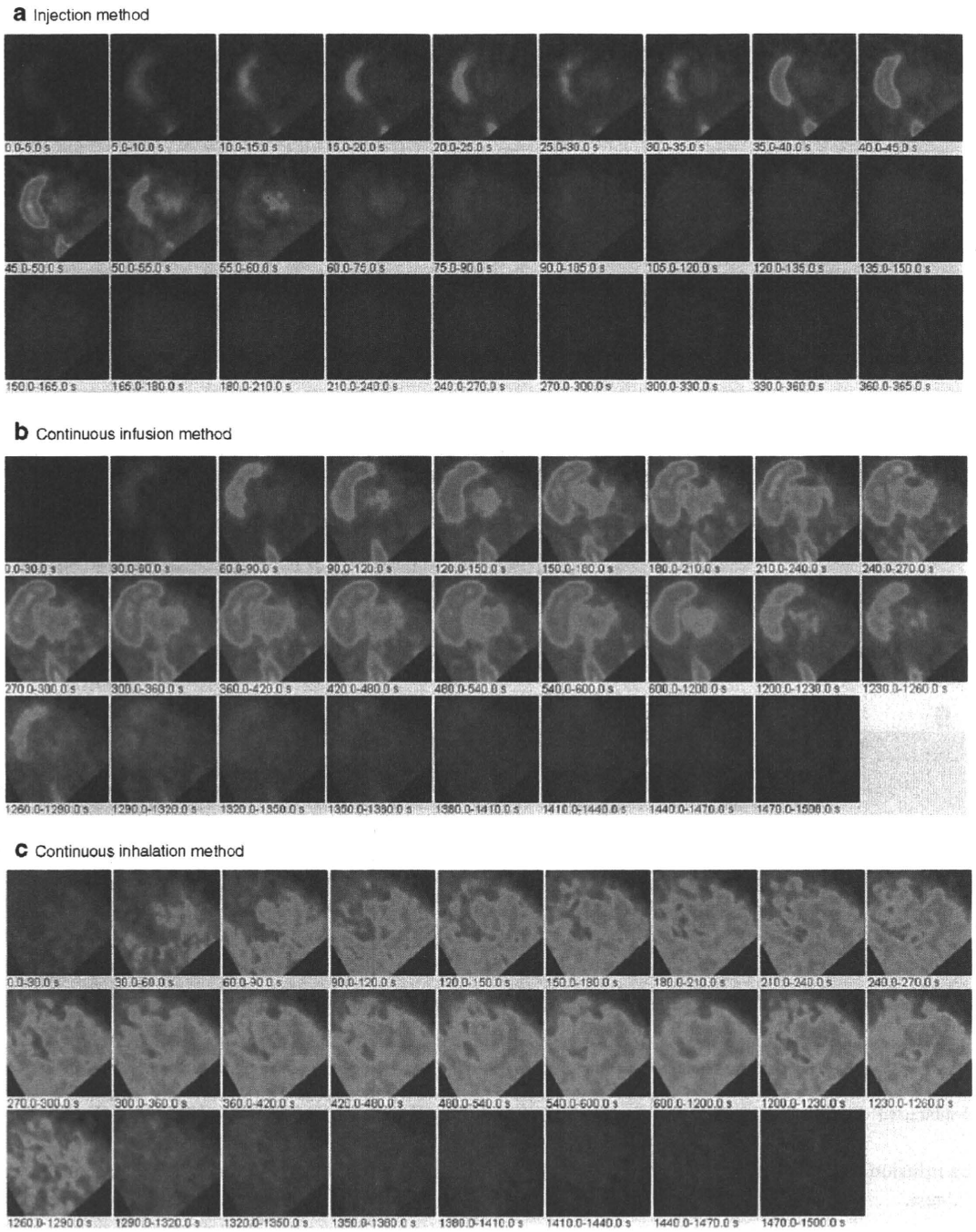

Fig. 2 PET images obtained in (**a**) the injection method, (**b**) the continuous-infusion method with injectable ^{15}O-O_2, and (**c**) the continuous-inhalation method with ^{15}O-O_2 gas

(Fig. 4b). The heart-to-lung radioactivity ratios were calculated from Fig. 4 for the quantitative estimation of image quality; the continuous-infusion method provided a ratio of 1.38±0.24, whereas the ratio was less than one with the continuous-inhalation method.

Table 2 shows the quantitative OEF values in the lateral wall obtained by the injection, continuous-infusion, and continuous-inhalation methods. These OEF values were consistent among the three methods.

Figure 5 represents the noise equivalent counts (NEC) standardized by the total counts detected by the PET scanner. Although the injection method tended to show rather high values, there was no significant difference between the values obtained by the injection and

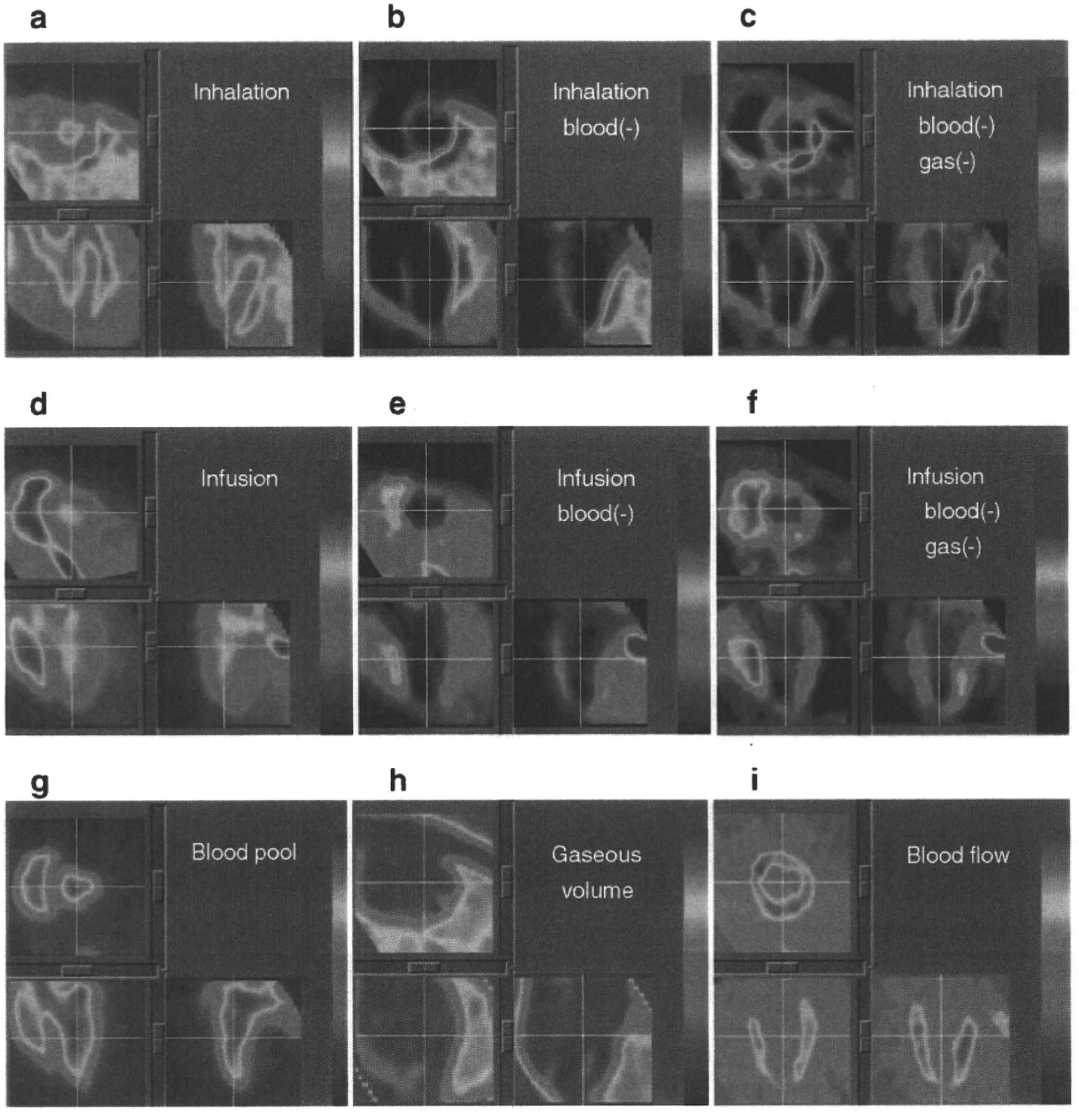

Fig. 3 PET images obtained in the study are shown. The 16th frame (steady-state frames) of the continuous-inhalation method and the continuous-infusion method are shown in (**a**) and (**d**), respectively. The 'blood-subtracted' images shown in (**b**) and (**e**) were created by subtraction of the blood-pool image by ^{15}O-CO (**g**) from (**a**) and (**d**). The 'blood- and gas-subtracted' images shown in (**c**) and (**f**) were created by the successive subtraction of the gaseous image (**h**) from (**b**) and (**e**). The myocardial blood flow image is also shown in (**i**)

continuous-infusion methods as determined by a Mann Whitney *U*-test.

Discussion

In previous studies, we showed the usefulness of the injectable ^{15}O-O_2 system for estimating cerebral oxygen metabolism in small animals such as rats under normal or ischemic conditions [10–12]. Injectable ^{15}O-O_2 replaced the inhalation protocol and radioactive ^{15}O-O_2 was administered via the tail vein. Thus, injectable ^{15}O-O_2 could abolish the artifact from the high radioactivity in the inhalation tube that distorts the PET images, especially in small animals. We considered that the concept could also be utilized in the hearts of large animals. Therefore, in the present study, we tested the feasibility of an injectable ^{15}O-O_2 system for estimating myocardial oxygen metabolism in normal pigs. In addition, since a shunt between the femoral artery and vein can be created in pigs but not in small animals, continuous infusion via the femoral shunt was also performed to achieve a constant and reliable delivery of radioactivity to the heart.

Dynamic PET scans showed a large difference in the radioactivity distribution among the three methods. Since the labeling efficiency to prepare injectable ^{15}O-O_2 was

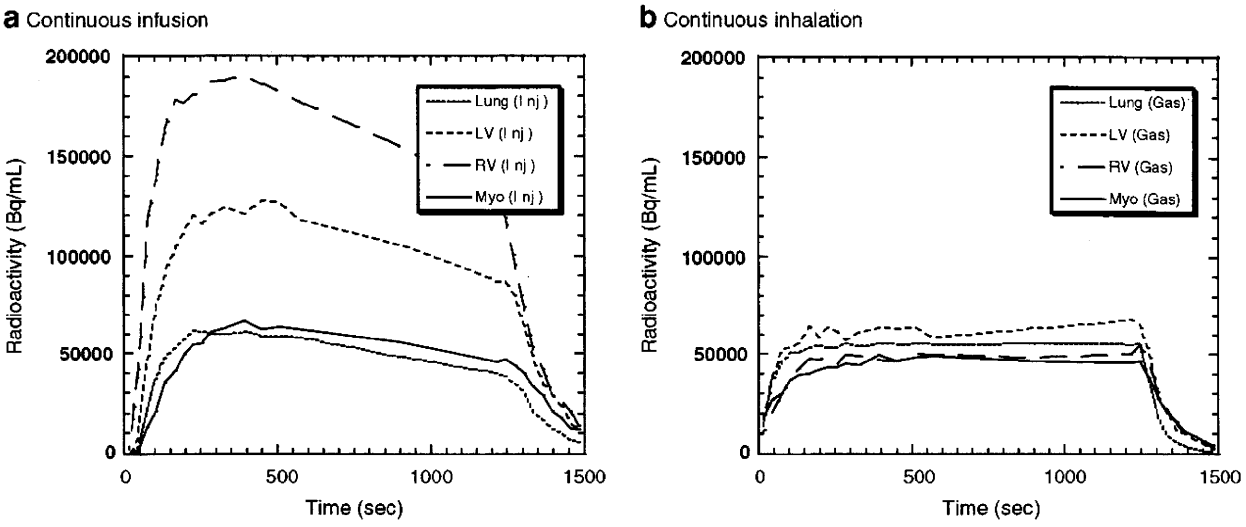

Fig. 4 Time-activity curves from the left ventricle (*LV*), the right ventricle (*RV*), the myocardium (lateral wall, Myo) and a lung region with the continuous-infusion method (**a**) and the continuous-inhalation method (**b**). The supply of radioactivity was started at time 0 s and stopped at 1,200 s. The 16th frame for the steady-state analysis was 600–1,200 s

lower with pig blood (ca. 61 MBq/ml at most) than with the blood of rats and humans (130 MBq/ml), the injection method provided rather obscure images. With the injection and continuous-infusion methods, the radioactivity in the lung was dramatically reduced in comparison to the continuous-inhalation method, since the heart-to-lung ratio with the continuous-infusion method was about 40% higher than with the continuous-inhalation method. This finding suggested that the two methods that inject radioactivity via a vein are more useful for analyzing myocardial oxygen metabolism in pigs than the continuous-inhalation method. However, a distinct difference between radioactivity of the right and left ventricles was observed in the images and time-radioactivity curves after venous administration of ^{15}O-O_2, indicating a certain degree of excretion of the radioactivity by the lung. Therefore, the spillover from the pulmonary alveoli to the myocardium could not be omitted in the two methods with venous administration, and Eq. (4) was used for the OEF analysis, although the radioactivity in the lung was lower than that in the myocardium.

On the other hand, with the continuous-inhalation method, the radioactivity of the lung was in between the radioactivity in the RV and LV. This is curious because O-15 radioactivity was supplied from the inhalation tube and transferred from the lung to blood so that the radioactivity in the lung should have been the highest among the four ROIs. This may have been caused, in part, by inhomogeneous distribution of the radioactivity in the lung due to its structure in comparison with the myocardium and ventricles, and/or by artifacts from the lung to other

Table 2 OEF estimated by the three methods using injectable ^{15}O-O_2 or ^{15}O-O_2 gas

	OEF		
	Injection	Infusion	Inhalation
Pig. 1	0.70	0.72	
Pig. 2	0.67	0.72	
Pig. 3	0.71	0.74	
Pig. 4	0.76	0.69	0.72
Average	0.71	0.72	0.72
SD	0.036	0.020	

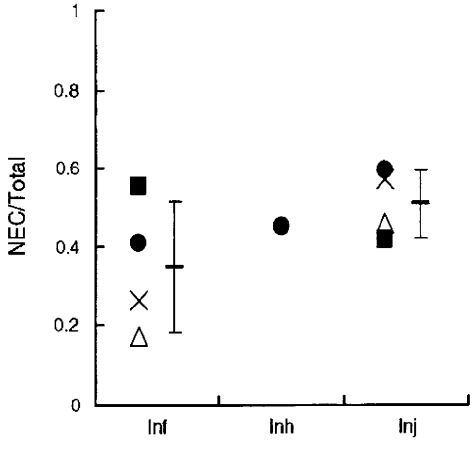

Fig. 5 The ratio of noise equivalent counts (*NEC*) to total counts in the total field of view of the PET scanner obtained with the continuous-infusion method (*Inf*), the continuous-inhalation method (*Inh*) and the injection method (*Inj*)

tissues. In any case, it is notable that the radioactivity in the myocardium was the lowest with the continuous-inhalation method, leading to difficulty in analyzing myocardial oxygen metabolism.

The OEF values in lateral walls were calculated to compare the ability of the three methods to determine myocardial oxygen metabolism by using the blood flow derived from the dual-administration protocol with the injection method and the single-administration protocol with the two continuous methods. There was no difference in the blood flow between the two protocols. Consequently, the three methods provided the same OEF value of about 0.7 and this is a physiological value in normal pigs, as was previously demonstrated [17, 18]. We have demonstrated the potential of the injectable ^{15}O-O_2 system for the estimation of physiological cerebral oxygen metabolism in rats and monkeys during early and late ischemia, hypertension, and ischemia plus hypertension [10–12, 19]. Therefore, we believe that the injection and continuous-infusion methods provide a physiological OEF in the myocardium. Nevertheless, we recognize the necessity to evaluate the reliability and usefulness of the injectable ^{15}O-O_2 method in myocardial applications. Further studies using pathophysiological animal models are required in the future, such as myocardial ischemia, hypoxia, and heart failure. On the other hand, since $MMRO_2$ is basically regarded as the product of MBF and OEF, the results indicated that these three methods were equivalent in their ability to quantify $MMRO_2$ in normal pigs, at least in the lateral wall. Although the images after the subtraction of spillovers from blood and gas showed different contrast between the continuous-infusion and continuous-inhalation methods, the ability of these two methods to measure OEF and $MMRO_2$ in the lateral walls was equivalent.

We did not evaluate myocardial oxygen metabolism in other heart regions since the radioactivity in the right ventricle could not be removed due to a significant difference of radioactivity between the ventricles with the continuous-infusion method. The injection method might be able to evaluate oxygen metabolism in other regions besides the lateral wall, although this was not evaluated in this study due to the low radioactivity of injectable ^{15}O-O_2 as described above. In the injection method, O-15 radioactivity was delivered from the femoral vein to RV, the lung, LV, and finally the myocardium. Thus, when the LV and myocardial activity reach a maximum, the RV activity is expected to be low. The later frames of the dynamic PET images with the injection method might avoid the high RV activity and delineate the myocardium and LV more clearly. With accurate anatomical information by gated PET/CT, the injection method will provide oxygen metabolism in other heart regions. In addition, the injection method has a benefit in that it is noninvasive and shortens the acquisition time in comparison with the continuous-infusion method. Future studies are needed to determine whether the injectable ^{15}O-O_2 system can be used in other heart regions.

With the injection method, the ratio of noise equivalent counts (NEC) to total counts tended to be the higher, probably because of the absence of high radioactivity adjacent to the PET scanner. Nevertheless, the continuous-infusion method did not show this tendency. This may be because tubes for the input to the artificial lung were positioned at the femoral shunt and the output to the drain of O-15 gas was positioned alongside the PET scanner, resulting in an increase of random counts during the study. Also, it is notable that the value with the continuous-inhalation method was not small, which suggests that the inhalation protocol itself did not worsen the results, but rather the high radioactivity in the lung might affect the analysis. In any case, if more care is given to shielding of the radioactivity in tubes and/or for arrangement of instruments in the PET room, a higher value of NEC/total counts will be obtained with the injectable ^{15}O-O_2 system.

The declining slope delineated in the time-activity curves with the continuous-infusion method requires some explanation. Since the flow rate of O-15 gas supply to the artificial lung positioned at the femoral shunt was maintained constant during the PET scan, it is possible that a decrease of labeling efficiency of the artificial lung occurred due to the deposition of any components of blood. The blood of rats or humans was negligibly deposited in the artificial lung during circulation at the same rate for at least 30 min in our other experiments, so that this problem may be specific for pigs. It is unclear which component in pig blood was exactly involved in the deposition and three of four pigs did not show a declining slope of the time-activity curve.

In practice, in routine studies on myocardial oxygen metabolism using large animals such as pigs, the continuous-inhalation method with ^{15}O-O_2 gas may be easier to perform for the following reasons: (1) the intubation tube used for gas anesthesia prior to the PET scan can also be used for ^{15}O-O_2 gas inhalation; (2) catheterization of the femoral artery and vein to create the femoral shunt for the continuous-infusion method may be troublesome; and (3) the injection of ^{15}O-O_2 requires an artificial lung, preparation time, and blood taken from the same animal prior to the PET scan. However, the injection of ^{15}O-O_2 has a substantial advantage over the continuous-inhalation method in that there is reduced radioactivity in the lung and clearer images of the heart are obtained. Therefore, the method for estimating myocardial oxygen metabolism should be selected depending on the objectives of the study and the surgical procedures. Furthermore, since radioactivity administered into the femoral vein is partially excreted into expired air, the injectable ^{15}O-O_2 system might be used for evaluating pulmonary function in the future.

Conclusion

In this study, we tested the feasibility of using an injectable ^{15}O-O_2 system to estimate myocardial oxygen metabolism in pigs. Both the bolus-injection and continuous-infusion methods reduced the radioactivity in the lung and provided similar OEF values in the lateral walls of the heart. These findings indicate that the injectable ^{15}O-O_2 system has the potential to evaluate myocardial oxygen metabolism.

References

1. Ohtake T. The review of myocardial positron emission computed tomography and positron imaging by gamma camera. Kaku Igaku. 1998;35:179–87.
2. Klein LJ, Visser FC, Knaapen P, Peters JH, Teule GJ, Visser CA, et al. Carbon-11 acetate as a tracer of myocardial oxygen consumption. Eur J Nucl Med. 2001;28:651–68.
3. Schelbert HR. PET contributions to understanding normal and abnormal cardiac perfusion and metabolism. Ann Biomed Eng. 2000;28:922–9.
4. Visser FC. Imaging of cardiac metabolism using radiolabelled glucose, fatty acids and acetate. Coron Artery Dis. 2001;12(Suppl 1):S12–8.
5. Hata T, Nohara R, Fujita M, Hosokawa R, Lee L, Kudo T, et al. Noninvasive assessment of myocardial viability by positron emission tomography with ^{11}C acetate in patients with old myocardial infarction. Usefulness of low-dose dobutamine infusion. Circulation. 1996;94:1834–41.
6. Yamamoto Y, de Silva R, Rhodes CG, Iida H, Lammertsma AA, Jones T, et al. Noninvasive quantification of regional myocardial metabolic rate of oxygen by $^{15}O_2$ inhalation and positron emission tomography. Experimental validation. Circulation. 1996;94:808–16.
7. Iida H, Rhodes CG, Araujo LI, Yamamoto Y, de Silva R, Maseri A, et al. Noninvasive quantification of regional myocardial metabolic rate for oxygen by use of $^{15}O_2$ inhalation and positron emission tomography. Theory, error analysis, and application in humans. Circulation. 1996;94:792–807.
8. Shidahara M, Watabe H, Kim KM, Oka H, Sago M, Hayashi T, et al. Evaluation of a commercial PET tomograph-based system for the quantitative assessment of rCBF, rOEF and $rCMRO_2$ by using sequential administration of ^{15}O-labeled compounds. Ann Nucl Med. 2002;16:317–27.
9. Mintun MA, Raichle ME, Martin WR, Herscovitch P. Brain oxygen utilization measured with O-15 radiotracers and positron emission tomography. J Nucl Med. 1984;25:177–87.
10. Magata Y, Temma T, Iida H, Ogawa M, Mukai T, Iida Y, et al. Development of injectable O-15 oxygen and estimation of rat OEF. J Cereb Blood Flow Metab. 2003;23:671–6.
11. Temma T, Magata Y, Kuge Y, Shimonaka S, Sano K, Katada Y, et al. Estimation of oxygen metabolism in a rat model of permanent ischemia using positron emission tomography with injectable ^{15}O-O_2. J Cereb Blood Flow Metab. 2006;26:1577–83.
12. Temma T, Kuge Y, Sano K, Kamihashi J, Obokata N, Kawashima H, et al. PET O-15 cerebral blood flow and metabolism after acute stroke in spontaneously hypertensive rats. Brain Res. 2008;1212:18–24.
13. Watabe H, Jino H, Kawachi N, Teramoto N, Hayashi T, Ohta Y, et al. Parametric imaging of myocardial blood flow with ^{15}O-water and PET using the basis function method. J Nucl Med. 2005;46:1219–24.
14. Iida H, Rhodes CG, de Silva R, Yamamoto Y, Araujo LI, Maseri A, et al. Myocardial tissue fraction–correction for partial volume effects and measure of tissue viability. J Nucl Med. 1991;32:2169–75.
15. Wienhard K, Dahlbom M, Eriksson L, Michel C, Bruckbauer T, Pietrzyk U, et al. The ECAT EXACT HR: performance of a new high resolution positron scanner. J Comput Assist Tomogr. 1994;18:110–8.
16. Kudomi N, Hayashi T, Teramoto N, Watabe H, Kawachi N, Ohta Y, et al. Rapid quantitative measurement of $CMRO_2$ and CBF by dual administration of ^{15}O-labeled oxygen and water during a single PET scan-a validation study and error analysis in anesthetized monkeys. J Cereb Blood Flow Metab. 2005;25:1209–24.
17. Alders DJ, Groeneveld AB, de Kanter FJ, van Beek JH. Myocardial O_2 consumption in porcine left ventricle is heterogeneously distributed in parallel to heterogeneous O_2 delivery. Am J Physiol Heart Circ Physiol. 2004;287:H1353–61.
18. Van Woerkens EC, Trouwborst A, Duncker DJ, Koning MM, Boomsma F, Verdouw PD. Catecholamines and regional hemodynamics during isovolemic hemodilution in anesthetized pigs. J Appl Physiol. 1992;72:760–9.
19. Temma T, Magata Y, Iida H, Hayashi T, Ogawa M, Mukai T, et al. Development of injectable O-15 oxygen and its application for estimation of OEF. International Congress Series, Quantitation in Biomedical Imaging with PET and MRI Proceedings of the International Workshop on Quantitation in Biomedical Imaging with PET and MRI. 2004;1265:262–65.

Journal of Cerebral Blood Flow & Metabolism (2010) 30, 663–673

www.jcbfm.com

Measurement of density and affinity for dopamine D_2 receptors by a single positron emission tomography scan with multiple injections of [^{11}C]raclopride

Yoko Ikoma[1,2], Hiroshi Watabe[1], Takuya Hayashi[1], Yoshinori Miyake[1], Noboru Teramoto[1], Kotaro Minato[2] and Hidehiro Iida[1]

[1]*Department of Investigative Radiology, National Cardiovascular Center Research Institute, Osaka, Japan;* [2]*Biomedical Imaging and Informatics, Graduate School of Information Science, Nara Institute of Science and Technology, Nara, Japan*

Positron emission tomography (PET) with [^{11}C]raclopride has been used to investigate the density (B_{max}) and affinity (K_d) of dopamine D_2 receptors related to several neurological and psychiatric disorders. However, in assessing the B_{max} and K_d, multiple PET scans are necessary under variable specific activities of administered [^{11}C]raclopride, resulting in a long study period and unexpected physiological variations. In this paper, we have developed a method of multiple-injection graphical analysis (MI-GA) that provides the B_{max} and K_d values from a single PET scan with three sequential injections of [^{11}C]raclopride, and we validated the proposed method by performing numerous simulations and PET studies on monkeys. In the simulations, the three-injection protocol was designed according to prior knowledge of the receptor kinetics, and the errors of B_{max} and K_d estimated by MI-GA were analyzed. Simulations showed that our method could support the calculation of B_{max} and K_d, despite a slight overestimation compared with the true magnitudes. In monkey studies, we could calculate the B_{max} and K_d of diseased or normal striatum in a 150 mins scan with the three-injection protocol of [^{11}C]raclopride. Estimated B_{max} and K_d values of D_2 receptors in normal or partially dopamine-depleted striatum were comparable to the previously reported values.

Journal of Cerebral Blood Flow & Metabolism (2010) **30,** 663–673; doi:10.1038/jcbfm.2009.239; published online 11 November 2009

Keywords: [^{11}C]raclopride; dopamine D_2 receptors; graphical analysis; multiple injections; positron emission tomography

Introduction

Positron emission tomography (PET) with [^{11}C]raclopride has been widely used to investigate the availability of striatal dopamine D_2 receptors *in vivo* (Farde *et al*, 1985; Köhler *et al*, 1985; Hall *et al*, 1988). A number of postmortem studies have shown that the abundance of dopamine D_2 receptor is elevated in striatum samples from untreated patients with Parkinson's disease (Guttman and Seeman, 1985; Seeman *et al*, 1987) and in schizophrenic patients who had never taken antipsychotics (Cross *et al*, 1981; Joyce *et al*, 1988). The PET measurements have made it possible to quantify *in vivo* the density and apparent affinity of receptors by systematically varying the specific activity (or mass) of an administered radioligand (see for example, Farde *et al*, 1986). A study of Parkinson's disease by Rinne *et al* (1995) with *in vivo* PET showed increased density and unchanged affinity of dopamine D_2 receptors in the putamen in comparison with healthy controls. In corresponding studies of schizophrenia, early findings with [^{11}C]*N*-methylspiperone indicated elevated D_2 binding, which was not replicated in some subsequent studies with [^{11}C]raclopride (Wong *et al*, 1986; Farde *et al*, 1987, 1990). Dysfunction of dopamine receptors has also been suggested in other neurodegenerative or psychiatric diseases (e.g., multiple-system atrophy, progressive supranuclear palsy, and attention-deficit hyperactivity disorders); however, there have been only a few studies that

Correspondence: Dr H Watabe, Department of Investigative Radiology, National Cardiovascular Center Research Institute, 5-7-1, Fujishirodai, Suita, Osaka 565-8565, Japan.
E-mail: watabe@ri.ncvc.go.jp
Received 11 September 2009; revised 13 October 2009; accepted 19 October 2009; published online 11 November 2009

examined receptor function directly related to density and affinity. This might be due to the inherent difficulty in measuring absolute receptor abundance based on PET recordings.

In PET scans, to determine the density and affinity of receptors directly as parameters of kinetic model, it is necessary to apply a compartmental analysis based on a two-tissue compartment five-parameter model including density of receptors B_{max} (pmol/mL), bimolecular association rate constant k_{on} (mL/pmol/min), and unimolecular dissociation rate constant k_{off} (min^{-1}) (Farde *et al*, 1989). However, since data from a single PET scan are not enough to determine the B_{max} and k_{on} individually, multiple PET scans should be taken with different molar amounts of injected ligand. In addition, model parameters are estimated by a nonlinear least squares fitting with the metabolite-corrected plasma input function, so the solutions are often unstable and sensitive to statistical noise, and invasive arterial sampling is required to use this method.

Farde *et al* (1986, 1989) determined the value of B_{max} and apparent affinity K_d ($=k_{off}/k_{on}$) by a graphical analysis using a time-activity curve (TAC) of the specifically bound target region and a reference region where specific bindings are negligible. In this method, the ratio of specific bound and free ligand concentrations at the equilibrium state are plotted versus the concentration of specific bound ligand, and B_{max} and K_d are estimated from the slope and intercept of the regression line. Other groups also used the value of distribution volume ratio − 1 estimated from the graphical analysis of Logan *et al* (1996), instead of the ratios of specific bound and free concentration, to obtain stable values of the *y*-axis quantity (Logan *et al*, 1997; Doudet and Holden, 2003; Doudet *et al*, 2003). These methods are practical, because they do not require arterial blood sampling, and their respective estimation processes are easy to carry out. However, to estimate the regression line of a graphical plot, multiple PET scans (at least two or three) are required under variable molar amounts of administered ligand, so scans have been performed on separate days. Even in quantitative PET scans, the separate day protocol may suffer from interday or intraday variations in physiologic conditions, such as cerebral blood pressure, flow, and receptor bindings, which may affect the accuracy of the estimates.

We developed a method, called the multiple-injection simplified reference tissue model (MI-SRTM), to measure the change in binding potential ($BP_{ND}=k_3/k_4$ (Mintun *et al*, 1984)) of dopamine D_2 receptors from a single session of PET scanning with multiple injections of [^{11}C]raclopride (Watabe *et al*, 2006; Ikoma *et al*, 2009), and we showed that this method could detect the change in BP_{ND} because of an increase in mass of administered [^{11}C]raclopride in a short scanning period, which is a prerequisite for measuring the saturation binding parameters as steady state. In this study, we extend our earlier report for estimating B_{max} and K_d from a single session of PET scanning with triple injections of [^{11}C]raclopride using MI-SRTM and the graphical analysis, and we validated the proposed method by performing numerous simulations and studies on monkeys using PET and [^{11}C]raclopride.

Materials and methods

Theory

Graphical Analysis with a Reference Region for Estimation of Density and Affinity: Graphical analysis based on the Scatchard plot (Scatchard, 1949) has been used to estimate the values of B_{max} and K_d from as series of PET recordings with various molar amounts of administered ligand (Farde *et al*, 1986). In brief, the ratios (B/F) of specific bound ligand concentration (B [pmol/mL]) and free ligand concentration (F [pmol/mL]) at equilibrium are plotted versus B. In this plot, the slope and *x*-intercept represent $-1/K_d$ and B_{max}, respectively. In general, for graphical analysis without arterial blood sampling, the total radioligand concentration in the reference region (C_r [Bq/mL]), where specific bindings are negligible, is used as an estimate of the free radioligand concentration in the target region (C_f [Bq/mL]), that is $C_f^{ref}=C_r$, and the specific binding radioligand concentration in the target region (C_b [Bq/mL]) is defined as radioactivity in the target region (C_t [Bq/mL]) reduced with C_r, that is $C_b^{ref}=C_t-C_r$ (Figure 1). The radioactivity concentrations of C_f^{ref} and C_b^{ref}, at the point in time when dC_b^{ref}/dt is 0 (T_{eq}), are divided by a specific activity of the administered ligand, and used as F and B at the transient equilibrium in the graphical analysis

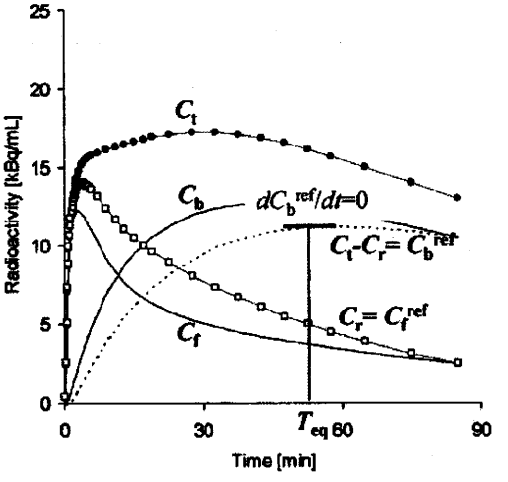

Figure 1 An example of simulated TACs for the striatum (C_t), free (C_f), and specific bound (C_b) concentrations in the striatum, the cerebellum used as a reference region (C_r) and bound concentration in the striatum estimated using a reference region ($C_b^{ref}=C_t-C_r$) with $K_1=0.033$, $K_1/k_2=0.59$, $k_{on}=0.0033$, $B_{max}=25.7$, $k_4=0.034$ for the striatum, and $K_1=0.034$, $K_1/k_2=0.36$, $k_3=0.022$, $k_4=0.034$ for the cerebellum. The time point of $dC_b^{ref}/dt=0$ (T_{eq}) is considered the transient equilibrium, and bound concentration at the equilibrium (B^{ref}) is obtained from the radioactivity concentration of C_b^{ref} at T_{eq}.

(Farde *et al*, 1989). In our study, we use the nomenclature B^{ref} and F^{ref} to represent the concentrations otherwise known as B and F. The value of the y axis, B^{ref}/F^{ref}, is sometimes replaced by the binding potential estimated by the graphical analysis of Logan *et al* (1996) or some other method (Logan *et al*, 1997; Doudet and Holden, 2003; Doudet *et al*, 2003).

Multiple-Injection Simplified Reference Tissue Model for Estimation of Binding Potential: A simplified reference tissue model (SRTM) can provide three parameters (R_1, k_2, BP_{ND}) without invasive arterial blood sampling by using a TAC of the reference region (Lammertsma and Hume, 1996). The MI-SRTM extended this SRTM for sequential multiple injections in a single session of PET scanning by taking into account the residual radioactivity in the target tissue at the time of each injection. As such, the magnitude of BP_{ND} for the ith injection is described in the following terms (Ikoma *et al*, 2009):

$$C_{ti}(t) = R_{1i}C_{ri}(t) + \left(k_{2i} - \frac{R_{1i}k_{2i}}{1+BP_{NDi}}\right)e^{-\frac{k_{2i}}{1+BP_{NDi}}t} \otimes C_{ri}(t) + (C_{ti}(0) - R_{1i}C_{ri}(0))e^{-\frac{k_{2i}}{1+BP_{NDi}}t} \quad (1)$$

where C_{ti} and C_{ri} are the radioactivity concentrations in the target and reference region, respectively, and t is the time from the start of the ith injection.

Multiple-Injection Graphical Analysis for Estimation of Density and Affinity: The conventional graphical analysis was applied to the B_{max} and K_d estimations with the multiple-injection approach. In this multiple-injection graphical analysis (MI-GA), the BP_{ND} calculated for each injection using MI-SRTM was plotted as a function of the concentration of specific bound raclopride at the transient equilibrium (B^{ref} [pmol/mL]) within the scan duration for each injection, and B_{max} and K_d were estimated from the regression line.

In this study for [^{11}C]raclopride, the TAC of the cerebellum was used as the reference TAC. Each parameter in the MI-SRTM was estimated by nonlinear least squares fitting with iteration of the Gauss–Newton algorithm. It should be noted that the transient equilibrium condition is required for each injection in the MI-GA.

Simulation Analysis

Simulations were performed to determine the range of administered mass of three injections and to evaluate feasibility of the MI-GA to estimate the B_{max} and K_d.

Effect of Injected Mass on BP_{ND} Estimates: To investigate the effect of the administered molar amount of [^{11}C]raclopride on BP_{ND} estimates and to determine the molar amount of three injections for monkey studies, a relationship between BP_{ND} and B^{ref} was obtained by a computer simulation. Noiseless TACs of the striatum and cerebellum were generated with a measured plasma TAC and assumed parameter values derived from measurements taken from the monkey studies. The TAC of the cerebellum was simulated with a conventional two-tissue compartment four-parameter model with assumed parameter values obtained earlier in our monkey studies: $K_1 = 0.034$ (mL/mL/min) $K_1/k_2 = 0.36$, $k_3 = 0.022$ (min^{-1}), $k_4 = 0.034$ (min^{-1}). Meanwhile, the TAC of the striatum was simulated with a two-tissue compartment five-parameter model expressed as Equation (2) by solving these differential equations with the numerical analysis of fourth-order Runge–Kutta method with assumed parameter values $K_1 = 0.033$ (mL/mL/min), $K_1/k_2 = 0.59$, $k_{on} = 0.0033$ (mL/pmol/min), $B_{max} = 25.7$ (pmol/mL), $k_4 = 0.026$ (min^{-1}), and SA = 37 (GBq/μmol):

$$\begin{aligned} \frac{dC_f}{dt} &= K_1C_p(t) - \left(k_2 + k_3'(t)\right)C_f(t) + k_4C_b(t) \\ \frac{dC_b}{dt} &= k_3'(t)C_f(t) - k_4C_b(t) \\ k_3'(t) &= k_{on}\left(B_{max} - \frac{C_b(t)}{SA}\right) \end{aligned} \quad (2)$$

where C_f and C_b are the concentrations of radioactivity for free and specifically bound [^{11}C]raclopride in tissue, respectively; and SA is the specific activity of administered [^{11}C]raclopride.

As reference, the relationships between B^{ref} and BP_{ND} or B^{ref}/F^{ref} were investigated in the case of a single injection of [^{11}C]raclopride by varying injected mass. TACs of the striatum and cerebellum for the single injection with a 50 mins scan were generated using the measured plasma TAC of a single injection in which the input plasma TAC was amplified, such that the corresponding mass increased from 1 to 500 nmol per injection. In each simulated TAC, BP_{ND} values were estimated by the SRTM, and then, B^{ref}/F^{ref} and B^{ref} were calculated by the transient equilibrium with the cerebellum TAC.

Next, TACs of the striatum and cerebellum for three injections at 50 mins intervals were generated using the plasma TAC of three sequential injections in which the input plasma TAC was amplified so that the mass of the first and second injections would be 1.5 and 10 nmol/kg, and the mass of the third injection would be 1.5 to 150 nmol/kg. In each simulated TAC, BP_{ND} values were estimated by the MI-SRTM, and B^{ref}/F^{ref} and B^{ref} for the third injection was calculated by the transient equilibrium with the cerebellum TAC. The relationships between B^{ref} and BP_{ND} or B^{ref}/F^{ref} for the third injection were investigated, and compared with that for the single injection.

Estimation of B_{max} and K_d Values by the Multiple-Injection Graphical Analysis: The reliability of B_{max} and K_d estimates by the graphical analysis was investigated for the proposed sequential multiple-injection approach (single PET scan) and compared with that for the conventional nonsequential approach (three PET scans on different days, such that no residual mass remained). Noiseless TACs of the striatum and cerebellum were simulated using assumed parameters of the two-tissue compartment model mentioned above and the plasma input function for three injections in which the magnitude of each 'virtual' input function was adjusted so that the injection mass would be 1.5, 10, or 30 nmol/kg determined from the simulation study mentioned above, with 50 mins intervals as reported

by Ikoma *et al* (2009). In the striatum TACs, B_{max} values were varied from 10 to 50 pmol/mL at 5 pmol/mL intervals with other parameters fixed (K_d = 7.9 pmol/mL), or K_d was varied from 3 to 15 at 2 pmol/mL intervals by changing k_{on} with other parameters fixed (B_{max} = 25.7 pmol/mL). For each TAC, B_{max} and K_d were estimated by the MI-GA from three points obtained by MI-SRTM for the single PET scan approach and they were estimated by the graphical analysis from three points obtained by the conventional SRTM for the three PET scan approach. Then, estimates were compared with the true values. In the single PET scan approach, B_{max} and K_d were also estimated without reference TAC by the MI-GA from three points of BP_{ND} and B obtained by the two-tissue compartment four-parameter model with the plasma input function shown in the Appendix.

Analysis of Monkey Studies

PET studies were performed on three cynomolgus macaques (weight 6.9 ± 2.1 kg) with the multiple-injection approach. One animal (monN) was a healthy monkey aged 5 years, and the others had a syndrome acquired Parkinsonism. Of these, one (monUP, aged 7 years) had hemiparkinsonism induced by injecting the selective neurotoxin, *N*-methyl-4-pheny1-1,2,3,6-tetrahydropyridine (MPTP) (0.4 mg/kg) into the right carotid artery (Bankiewicz *et al*, 1986), whereas the other (monBP, aged 5 years) had bilateral Parkinsonism induced by injecting MPTP (0.4 mg/kg) intravenously and intermittently (twice a week for a total of 14 injections) (Takagi *et al*, 2005). Each Parkinsonian animal showed typical Parkinsonian symptoms in the limbs (motor slowness, tremor) unilaterally or bilaterally. The PET scan was performed after the symptom reaching stable (6 months after the first injection of MPTP). Anesthesia was induced with ketamine (8.4 mg/kg, intramuscularly) and xylazine (1.7 mg/kg, intramuscularly) and maintained by intravenous propofol (6 mg/kg/h) and vecuronium (0.02 mg/kg/h) during the scan. The monkeys were maintained and handled in accordance with guidelines for animal research on Human Care and Use of Laboratory Animals (Rockville, National Institutes of Health/Office for Protection from Research Risks, 1996). The study protocol was approved by the Subcommittee for Laboratory Animal Welfare of the National Cardiovascular Center.

After the synthesis of [^{11}C]raclopride, nonradioactive raclopride was added so that targeted molar amount of raclopride would be administered for three injections (1.5, 10, and 30 nmol/kg); this was done by dividing the [^{11}C]raclopride diluted by nonradioactive raclopride into three portions with different volumes, containing the intended masses of raclopride. For the first injection, 1.9 ± 0.16 nmol/kg (57.0 ± 5.7 MBq) of [^{11}C]raclopride was administered by a bolus injection at the beginning of the scan. Fifty minutes later, the second [^{11}C]raclopride injection, 11.1 ± 0.56 nmol/kg (60.4 ± 8.8 MBq at the time of second injection) was administered by a bolus, and 50 mins after that, a bolus of 31.1 ± 2.1 nmol/kg (30.8 ± 4.4 MBq at the time of third injection) of [^{11}C]raclopride was administered again. Data were acquired for 150 mins (10 secs × 18, 30 secs × 6, 120 secs × 7, 300 secs × 6; total 50 mins for each injection). The specific radioactivity was 4.7 ± 2.2 GBq/μmol at the time of the first injection.

PET scans were performed using a PCA-2000A positron scanner (Toshiba Medical Systems Corporation, Otawara, Japan) that provides 47 planes and a 16.2 cm axial field-of-view. The transaxial and axial spatial resolution of the PET scanner were 6.3 and 4.7 mm full width at half maximum (Herzog *et al*, 2004). A transmission scan with a 3-rod source of ^{68}Ge-^{68}Ga was performed for 20 mins for attenuation correction before the administration of [^{11}C]raclopride. Radioactivity was measured in the three-dimensional mode and the data were reconstructed by a filtered back-projection using a Gaussian filter (3 mm of full width at half maximum). Region-of-interests (ROIs) were defined manually over the left and right striatum and cerebellum for PET images, and the radioactivity concentrations in these regions were obtained. For the left and right striatum, R_1, k_2, and BP_{ND} for each injection were estimated by the MI-SRTM. In addition, parametric images were generated, estimating each parameter voxel by voxel, using the MI-SRTM with a basis function method in which the model Equation (1) was solved using linear least squares for a set of basis functions, which enables the incorporation of parameter bounds (Gunn *et al*, 1997; Ikoma *et al*, 2009). B_{max} and K_d were estimated by the MI-GA from these BP_{ND} values of left and right striatum for three injections.

In the unilateral Parkinsonian animal, three PET scans with conventional single injection with different masses of [^{11}C]raclopride were also performed for comparison with results by the multiple-injection single PET scan approach. A PET scan with a bolus injection of 2.1 nmol/kg (50.6 MBq), 11.3 nmol/kg (60.4 MBq), or 31.1 nmol/kg (30.8 MBq) of [^{11}C]raclopride was obtained on separate days. PET data were acquired for 50 mins with the same protocol as the single PET scan approach. The values of R_1, k_2, and BP_{ND} were estimated by the SRTM, and B_{max} and K_d were estimated by the conventional graphical analysis.

Results

Simulation Study

Effect of Injected Mass on BP_{ND} Estimates: In the simulations, the value of BP_{ND}, estimated by the MI-SRTM, decreased as injected molar amount of raclopride increased, that is, concentration of bound raclopride became larger. The relationship between BP_{ND} and B^{ref} had a good linear correlation to some extent; however, it did not remain linear for large B^{ref} (Figure 2A). The regression line where $B^{ref} < 20$ pmol/mL was $BP_{ND} = -0.091B^{ref} + 2.4$, $R^2 = 0.997$ for the first injection. In the relationship between BP_{ND} and B^{ref}, BP_{ND} values of the third injection were higher than those of the first injection when B^{ref} was lower than 20 pmol/mL. The ratio B^{ref}/F^{ref} was almost the same as the BP_{ND} estimated by MI-SRTM, though it was a little smaller when B^{ref} was lower than 5 pmol/mL (Figure 2B).

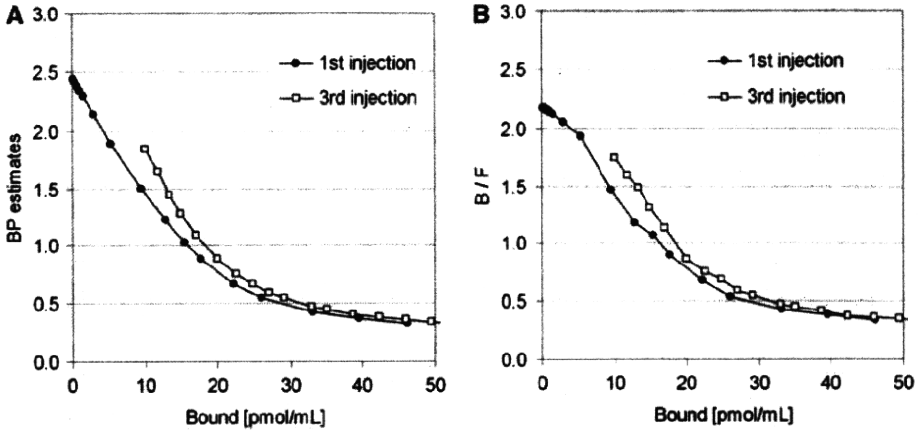

Figure 2 Relationship between specifically bound concentration and BP_{ND} **(A)** or B^{ref}/F^{ref} **(B)** estimates for the first and third injection in the simulations.

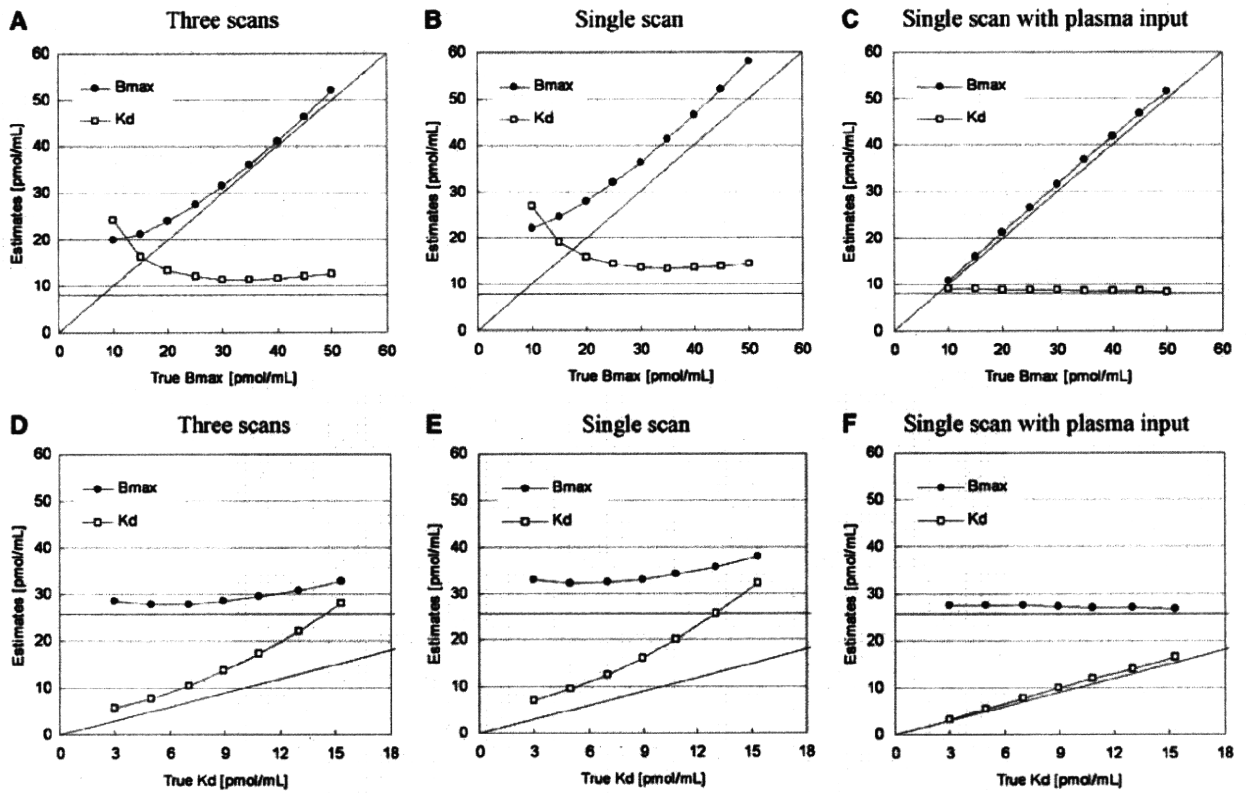

Figure 3 Relationships between estimates and true values of B_{max} and K_d for simulated TACs with various B_{max} and fixed K_d **(A–C)** and with various K_d and fixed B_{max} **(D–F)** by the three PET scan approach **(A, D)**, multiple-injection single PET scan approach **(B, E)**, and single PET scan approach with the plasma input function **(C, F)**.

Estimation of B_{max} and K_d Values by the Multiple-Injection Graphical Analysis: The TACs were calculated for a range of possible B_{max} and K_d values, and the relationship between true and estimated B_{max} or K_d values was investigated for conventional three PET scan and the proposed single PET scan approaches. When B_{max} was varied, B_{max} and K_d were overestimated compared with the true values in both three PET scan and single PET scan approaches (Figures 3A and 3B). However, a good correlation was observed between true and estimated B_{max}, and there was little variation in estimated K_d when B_{max} was set higher than 20 pmol/mL. Similarly, when K_d was varied, although K_d and B_{max} were overestimated in both approaches, there was a good correlation between true and estimated K_d, and estimated B_{max} was constant (Figures 3D and 3E). In both cases, B_{max} and K_d estimates in the single

PET scan approach were higher than those in the three PET scan approach. In the TAC simulated with $B_{max} = 25.7$ and $K_d = 7.0$, estimated B_{max} and K_d were 27.8 and 10.5, respectively, in the three PET scan approach, and 32.3 and 12.6, respectively, in the single PET scan approach. In contrast to these approaches with the reference TAC, the overestimation of B_{max} and K_d was scarcely observed in the MI-GA with the plasma input function (Figures 3C and 3F).

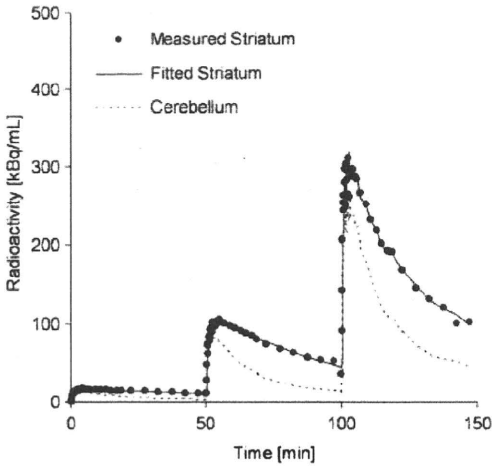

Figure 4 Measured TACs of the striatum and cerebellum and a fitted curve for the striatum using MI-SRTM in the monkey study by a single scan with sequential three injections of [^{11}C]raclopride.

Monkey Studies

Typical examples of TACs for the striatum and the cerebellum in the multiple-injection study are shown in Figure 4, and the parametric images of BP_{ND} for the first, second, and third injection, and images of B_{max} and K_d for the voxels in which BP_{ND1} was higher than 1.5 are shown in Figure 5. The estimated BP_{ND} decreased as the injected molar amount of [^{11}C]raclopride became larger in the second or third injection. Estimated BP_{ND1}, BP_{ND2}, and BP_{ND3} values were 2.3, 1.4, and 0.74, respectively, in the left striatum, and 2.6, 1.9, and 0.87, respectively, in the right striatum. The reduction in BP_{ND} was also observed in the parametric images.

The plots of MI-GA are shown in Figure 6. Plots of MI-GA for each of three animals were on the line, and B_{max} and K_d could be estimated as summarized in Table 1. Using the single scan approach for the hemiparkinsonian animal, B_{max} was 42.3 pmol/mL and K_d was 15.2 pmol/mL in the affected (right) striatum, and B_{max} was 32.3 pmol/mL and K_d was 13.0 pmol/mL in the contralateral (left) normal striatum. Corresponding estimates for the three scan approach were $B_{max} = 36.4$ and $K_d = 13.3$ pmol/mL in the right striatum and $B_{max} = 29.2$ and $K_d = 11.6$ pmol/mL in the

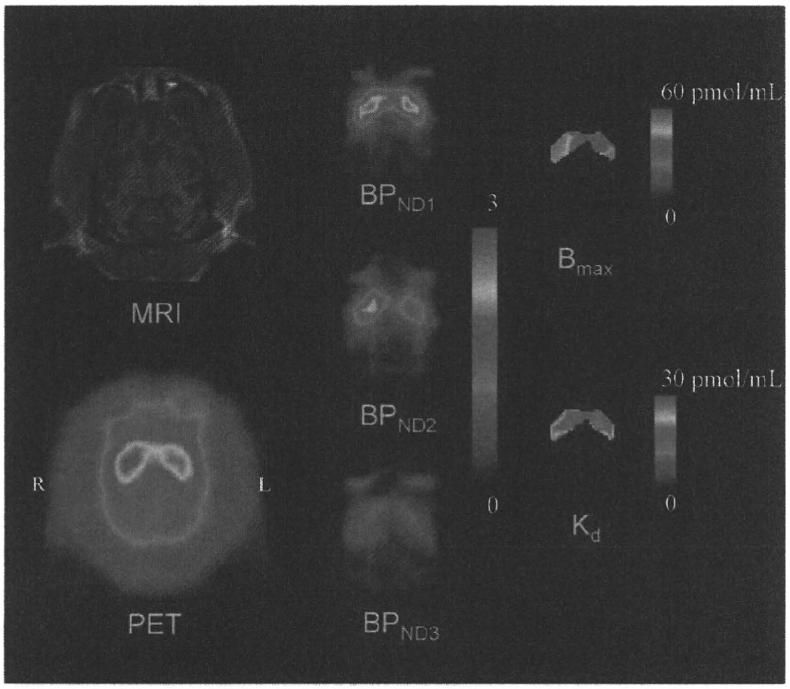

Figure 5 MRI and PET summation image (left) and parametric images of BP_{ND} for the first, second, and third injection (center) and parametric images of B_{max} and K_d for the voxels in which BP_{ND1} is higher than 1.5 (right) in the unilateral Parkinsonian (monUP) monkey study by a single scan with three sequential injections of [^{11}C]raclopride. Although ROI analysis disclosed higher B_{max} values in the MPTP-infused side of the striatum, the parametric image showed more evident increase of B_{max} in the dorsal and posterior parts of the striatum.